

Physical properties of transparent perovskite oxides (Ba,La)SnO₃ with high electrical mobility at room temperature

Hyung Joon Kim¹, Useong Kim², Tai Hoon Kim¹, Jiyeon Kim², Hoon Min Kim², Byung-Gu Jeon¹, Woong-Jhae Lee¹, Hyo Sik Mun², Kwang Taek Hong¹, Jaejun Yu², Kookrin Char^{2†} and Kee Hoon Kim^{1†}

¹*Center for Novel States Complex Materials Research, Department of Physics and Astronomy, Seoul National University, Seoul 151-747, Republic of Korea*

²*Center for Strongly Correlated Materials Research, Department of Physics and Astronomy, Seoul National University, Seoul 151-747, Republic of Korea*

ABSTRACT

Transparent electronic materials are increasingly in demand for a variety of optoelectronic applications, ranging from passive conductive leads to active thin film transistors. BaSnO₃ is a semiconducting oxide with a large band gap of more than 3.1 eV. Recently, we discovered that BaSnO₃ doped with a few percent of La exhibits unusually high electrical mobility of 320 cm²(Vs)⁻¹ at room temperature and superior thermal stability at high temperatures [H. J. Kim *et al.* Appl. Phys. Express. **5**, 061102 (2012)]. Following that work, we report here various physical properties of (Ba,La)SnO₃ single crystals and epitaxial films including temperature-dependent transport and phonon properties, optical properties and first-principles calculations. We find that almost doping-independent mobility of 200-300 cm²(Vs)⁻¹ is realized in the single crystals in a broad doping range from 1.0×10¹⁹ to 4.0×10²⁰ cm⁻³. Moreover, the conductivity of ~10⁴ Ω⁻¹cm⁻¹ reached at the latter carrier density is comparable to the highest value previously reported in the transparent conducting oxides. We attribute the high mobility to several physical properties of (Ba,La)SnO₃: a small effective mass coming from the ideal Sn-O-Sn bonding in a cubic perovskite network, small disorder effects due to the doping away from the SnO₂ conduction channel, and reduced carrier scattering due to the high dielectric constant. The observation of a reduced mobility of ~70 cm²(Vs)⁻¹ in the epitaxial films is mainly attributed to additional carrier-scattering due to dislocations and grain boundaries, which are

presumably created by the lattice mismatch between the substrate SrTiO₃ and (Ba,La)SnO₃. The main optical gap coming from the charge transfer from O 2*p* to Sn 5*s* bands in (Ba,La)SnO₃ single crystals remained at about 3.25 eV and the in-gap states only slightly increased, thus maintaining optical transparency in the visible spectral region. Based on all these results, we suggest that the doped BaSnO₃ system holds great potential for realizing all perovskite-based, transparent high-frequency high-power functional devices as well as highly mobile two-dimensional electron gas via interface control of heterostructured films.

PACS number: 81.05.Hd, 71.20.Nr, 72.10.Bg, 72.20.Dp, 78.40.Fy

I. INTRODUCTION

Transparent oxide materials offer great potential for a wide range of device applications, e.g. conducting leads for solar cells, flat panel displays, light emitting diodes, and transparent logic devices. Numerous oxide materials including ZnO, In₂O₃, and SnO₂ have been investigated for these purposes, successfully demonstrating passive conducting leads to active semiconducting devices such as *pn* junctions, field effect transistors, and UV lasers.¹⁻⁸ However, these well-known material systems still have limitations so that there is currently active scientific research to find alternative transparent materials which can potentially exhibit better physical properties. For example, high mobility is one essential ingredient for developing transparent logic devices with high density, and oxygen stability is also crucial to overcome interface degradation problems in the oxide *pn* junctions. Moreover, controlling and minimizing the density of defects or dislocations becomes also important to realize useful devices based on transparent conducting oxides (TCOs) and transparent oxide semiconductors (TOSs).

Oxide materials with the perovskite structure have exhibited a plethora of interesting physical properties such as superconductivity, colossal magnetoresistance, ferroelectricity, and piezoelectricity.⁹⁻¹² Extensive research efforts have been made to utilize such varied physical properties in the form of thin film heterostructures.¹³ The perovskite materials have also been investigated in the context of searching for new TCOs and TOSs as in doped SrTiO₃ and doped CaTiO₃.¹⁴⁻¹⁸ The alkaline earth stannates with a chemical formula *ASnO*₃ (*A* = Ba, Sr, and Ca) are another perovskite system that has been used in industry for photoelectrochemical energy conversions, stable capacitors, and gas sensors.¹⁹⁻²¹ In particular, BaSnO₃ is known to form an ideal cubic perovskite structure (See, Fig. 1(a)), in which the Sn-O-Sn bonding angle is close to 180°, and corresponds to a transparent, wide band gap semiconductor with an optical gap of ~ 3.1 eV.²² In order to have electrical conduction in BaSnO₃, both Ba and Sn sites were doped to form compounds like (Ba,La)SnO₃ and Ba(Sn,Sb)O₃ in polycrystalline or thin film forms.²³⁻²⁷ However, the reported

electrical mobility in the thin film was relatively low, less than $2 \text{ cm}^2(\text{Vs})^{-1}$ and the conductivity reached at most $500 \text{ } \Omega^{-1}\text{cm}^{-1}$.^{26,27} As those reported transport properties might not be intrinsic, possibly due to, e.g., grain boundary scattering or off-stoichiometry, the growth of high quality single crystals of doped BaSnO_3 and the study of their intrinsic physical properties are of high interest.

Recently, we succeeded in growing single crystals²⁸⁻²⁹ of $(\text{Ba,L a})\text{SnO}_3$ and $\text{Ba}(\text{Sn,Sb})\text{O}_3$ by the Cu_2O -flux method up to a lateral size of $\sim 2 \text{ mm}$. In particular, we discovered that a $(\text{Ba,L a})\text{SnO}_3$ single crystal shows an unprecedentedly high electrical mobility of $\sim 320 \text{ cm}^2(\text{Vs})^{-1}$ with a carrier density of $1.0 \times 10^{20} \text{ cm}^{-3}$ at room temperature.²⁸ In parallel with our discovery, there was a similar report on the growth of $(\text{Ba,L a})\text{SnO}_3$ single crystals by PbO and PbF_2 flux,³⁰ in which the highest electrical mobility was found to be $\sim 103 \text{ cm}^2(\text{Vs})^{-1}$. We also found that the epitaxial thin films of $(\text{Ba,L a})\text{SnO}_3$ grown on SrTiO_3 (001) substrate shows an electrical mobility as high as $70 \text{ cm}^2(\text{Vs})^{-1}$, which is much larger than the previously reported values^{26,27} in thin films. Moreover, the resistivity of the $(\text{Ba,L a})\text{SnO}_3$ film has shown little change even at $500 \text{ }^\circ\text{C}$ in air, which suggests extremely good oxygen stability and related physical properties at high temperatures.²⁸

In order to understand further the origins of such high mobility in the $(\text{Ba,L a})\text{SnO}_3$ system, we systematically report various physical properties of the single crystals and epitaxial films in the following sections. In Sec. II, we describe the various experimental tools we have employed. In Sec. III, we present experimental and theoretical results in wide doping ranges in the crystals and films, including temperature-dependent transport properties, structural characteristics, band structure calculations, and optical properties. From the Hall effect measurements in a broad doping range from 1.0×10^{19} to $4.0 \times 10^{20} \text{ cm}^{-3}$, we found that the mobility remains as high as $\sim 200\text{-}300 \text{ cm}^2(\text{Vs})^{-1}$ and does not show clear dependence on the carrier density. In Sec. IV, we discuss mainly the possible physical origins for obtaining the high electrical mobility. In Sec. V, we conclude that $(\text{Ba,L a})\text{SnO}_3$ has a great potential for being used as perovskite-based TOSs with high electrical mobility and superior thermal stability.

II. EXPERIMENTAL

For the single crystal growth of $\text{Ba}_{1-x}\text{La}_x\text{SnO}_3$ ($x = 0-0.04$), the corresponding polycrystalline specimen was first synthesized as a seed material. High purity BaCO_3 , SnO_2 , and La_2O_3 powders were weighed in a stoichiometric ratio, thoroughly mixed in an agate mortar, and fired at 1250°C for 6 hours. After several intermediate grindings, the powders were pressed into a pellet and sintered at $1400-1450^\circ\text{C}$ for 24-48 hours. For the growth of $(\text{Ba},\text{La})\text{SnO}_3$ single crystals, the Cu_2O flux and the sintered powder were placed in a Pt crucible with a molar ratio of about 15:1 and were fired in air above 1250°C and then slowly cooled down to 1210°C , followed by a slow furnace cooling to room temperature. The crystals show a cube-like shape as shown in Fig. 1(b).

We grew epitaxial films by use of the pulsed laser deposition technique, using BaSnO_3 , $\text{Ba}_{0.96}\text{La}_{0.04}\text{SnO}_3$, and $\text{Ba}_{0.93}\text{La}_{0.07}\text{SnO}_3$ targets. We used single crystal SrTiO_3 (001) as a substrate, and performed the deposition in an O_2 pressure of 100 mTorr at 750°C . After the deposition, we cooled the samples in an O_2 pressure of about 600 mTorr.

We investigated the structural properties of the poly- and single-crystalline samples by use of X-ray diffraction (XRD), for which we used a high power X-ray diffractometer equipped with a single $\text{Cu K}\alpha_1$ source (EmpyreanTM, PANalytical). We performed temperature-dependent X-ray diffraction measurements for the polycrystalline powder of $\text{Ba}_{0.999}\text{La}_{0.001}\text{SnO}_3$ by use of a closed-cycle cryostat (PheniXTM, Oxford Instruments), operating in the 20-300 K temperature range. We also characterized the structure of epitaxial films with a four-circle X-ray diffractometer.

The first-principles density functional theory (DFT) calculations were performed by using the Vienna *ab-initio* Simulation Package (VASP) code.³¹ The projector-augmented-wave (PAW) method³² and the Ceperley-Alder parameterization were employed within the local density approximation (LDA).³³ To determine the electronic structure of La-doped BaSnO_3 , we adopted a $3\times 3\times 3$ supercell containing 135 atoms and carried out the k -space integration using a $2\times 2\times 2$ mesh within the Monkhorst-Pack k -point sampling. For the calculations, all atomic coordinates were

relaxed and the Hellmann-Feynman force reached to less than 0.02 eV \AA^{-1} . The cut-off energy used for the plane wave basis set was 520 eV .

Temperature-dependent resistivity was measured by the conventional four-probe technique for the single crystals and films from 2 K to 300 K either in a closed cycle refrigerator or in a physical property measurement system (PPMSTM, Quantum Design). The five-wire configuration was employed to investigate the Hall effect in single crystals and some thin films as a function of temperatures in a magnetic field up to 9 tesla .

Optical transmission spectra were obtained in BaSnO_3 and $(\text{Ba,Lu})\text{SnO}_3$ ($n = 2.39 \times 10^{20} \text{ cm}^{-3}$) single crystals, which were optically polished to have thickness less than $100 \mu\text{m}$. The ultraviolet-visible-near infrared transmission spectra were measured by a fiber-optic spectrometer (StellaNet, EPP2000) equipped with a Xe-arc lamp as a light source. For the absorption coefficient (α), we repeated the transmission measurements of the same piece of sample in two different thicknesses and calculated α based on the formula $\alpha = -\ln(T_{\text{thick}}/T_{\text{thin}})/d$, where d is the thickness difference.

Heat capacity data of BaSnO_3 single crystals were measured by using a commercial calorimeter provided by PPMSTM (Quantum Design). A custom-made program was developed to perform a least-square-fitting based on the relaxation method with the lumped- τ_2 model,³⁴ which is often called as the curve fitting method.³⁵ Based on the fitting, we first extracted the addenda heat capacity of the calorimeter in a wide temperature range from 2 K to 340 K . After obtaining the addenda heat capacity, we subsequently measured the total heat capacity including the BaSnO_3 single crystal (total mass = 20.33 mg) and the addenda to extract eventually the heat capacity of the single crystal.

III. RESULTS

A. Chemical and structural properties

Figure 1 (c) shows the XRD pattern (θ - 2θ scan) of a typical $(\text{Ba,Lu})\text{SnO}_3$ single crystal after grinding into a fine powder form. The pattern reveals that the single crystal forms the cubic perovskite

phase without any detectable impurity phase. We have indeed tried to grow high quality single crystals by using various kinds of fluxes to investigate the intrinsic properties of La-doped BaSnO₃. Among those trials, we could also grow rather a large size BaSnO₃ single crystals ($\sim 2 \times 2 \times 1$ mm³) by using the mixed flux of PbO and PbF₂, which is similar to the recent report.³⁰ However, the EPMA (electron-probe-micro-analyses) study²⁸ showed that the grown single crystals using the Pb-containing flux unavoidably contained significant Pb impurities. On the other hand, the crystals grown by the Cu₂O flux did not contain any Cu related impurity according to the EPMA study. It is thus expected that our single crystals without any Cu impurity from the Cu₂O flux can offer a better chance to observe the intrinsic properties of (Ba,La)SnO₃.

In the case of (Ba,La)SnO₃ thin films, the XRD patterns in Fig. 1 (d) show the (00*l*) peaks, due to the epitaxial growth on SrTiO₃ (001) as demonstrated in the reciprocal mapping study in Ref. 28. The inset in Fig. 1 (d) shows that the full-width-at-half-maximum (FWHM) in the rocking curve is only 0.09°, supporting a high degree of crystallinity in our epitaxial film. It is worth mentioning that the FWHM in a previous report was about 0.57°,²⁶ which is much larger than that of our films. This experimental result suggests that the quality of the thin films should be superior to those studied in previous publications.^{26,27}

Figure 2 shows the variation of the lattice parameters of polycrystalline Ba_{1-x}La_xSnO₃ ($x = 0.00, 0.01, 0.02, \text{ and } 0.04$) as obtained from the Rietveld refinement of the powder diffraction data. It is noted that as the La concentration (x) increases, the lattice parameter increases almost linearly. It is rather unusual to find such an increase of the lattice parameter while doping by the La³⁺ ion, which has a smaller ionic radius (0.103 nm) than that of Ba²⁺ (0.135 nm).³⁶ We will discuss the origin of this unusual lattice expansion in Sec. IV.

B. First-principles calculations

Figure 3 presents the band structures of both BaSnO₃ and (Ba,La)SnO₃ as obtained by first-principles density functional theory (DFT) calculations with local density approximation (LDA). To our knowledge, the band structure calculation based on the LDA approximation was reported only for BaSnO₃,²² not for (Ba,La)SnO₃. The band structures of BaSnO₃ and (Ba,La)SnO₃ were drawn for the 3×3×3 supercell with 27 unit cells corresponding to the doping rate of $x = 0.037$ in Ba_{1-x}La_xSnO₃. According to the folded Brillouin zone of the 3×3×3 supercell as shown in Fig. 3 (a), BaSnO₃ seems to have an indirect band gap. Thus, the La-doping provides electron states directly well-inside the conduction band of BaSnO₃, which is mainly characterized as the Sn 5s states with the Sn-O antibonding character. This means that a La ion acts as an electron donor and its ionic valence becomes La³⁺. The occupation in the anti-bonding state is likely to result in repulsive forces between Sn and O to lower the total energy of the crystal structure, thereby inducing expansion of the lattice as seen in Fig. 2.

It is further noted that the electronic structure of BaSnO₃ has a highly dispersive conduction band, mainly composed of Sn 5s bands. The shape of the conduction band is indeed similar to the LDA result³⁷ of the In₂O₃, a mother compound of the well-known TCO material, In₂O₃:Sn. This observation indicates that similar to In₂O₃:Sn, there is a good possibility of obtaining highly mobile *n*-type carriers in BaSnO₃ as well upon doping La onto Ba sites. When the La doping is made to form (Ba,La)SnO₃, the Fermi level shifts into well inside the Sn 5s band (the dotted line in Fig. 3 (b)). The change of the band structure by La-doping is negligible near the Fermi level. The presence of La 4*f* bands at 2 eV above the Fermi level did not affect the band dispersion of the original conduction band of BaSnO₃. The calculated effective masses of the conduction band turn out to be about 0.4*m*₀ for both BaSnO₃ and (Ba,La)SnO₃, where *m*₀ is the free electron mass. The Fermi level of (Ba,La)SnO₃ in Fig. 3 (b) indicates that the 3.7 % La doped (Ba,La)SnO₃ is in a degenerately doped regime with *n*-type carriers which is consistent with the temperature-dependent transport results explained below.

C. Transport properties

Figure 4 summarizes the resistivity and mobility variation as a function of carrier density at room temperature in both single crystals and thin films. The data from our earlier report are also compared (closed squares and triangles). Previously,²⁸ we found that the mobility of single crystals is roughly proportional to n^{-1} , while the mobility of thin films is proportional to $n^{1/2}$ in a low doping range smaller than $n = 4 \times 10^{20} \text{ cm}^{-3}$. On the other hand, in the extended measurements for the single crystals of the present work in a broad doping range from 1.0×10^{19} to $4.0 \times 10^{20} \text{ cm}^{-3}$, we find that the measured electrical mobility values are instead scattered between 200 - 300 $\text{cm}^2(\text{Vs})^{-1}$ without showing clear dependence on the carrier density. It is noteworthy that the previous data for the single crystals (solid squares in Fig 4.) show rather large variation of mobility and reduced mobility at a high carrier density although the crystals come from the same batch. Thus, we tentatively presume that the crystals studied in Ref. 28 might have systematic increase of oxygen vacancy with carrier density increase. We note that the present newly updated mobility values still mark the highest record among the wide-band-gap oxide semiconductors in a similar doping level; e.g., highest known $\mu = \sim 160 \text{ cm}^2(\text{Vs})^{-1}$ for indium oxide (In_2O_3),³⁸ $\sim 50 \text{ cm}^2(\text{Vs})^{-1}$ for tin oxide (SnO_2),³⁹ and $\sim 100 \text{ cm}^2(\text{Vs})^{-1}$ for zinc oxide (ZnO).⁴⁰ We further note that, due to the high mobility of the $(\text{Ba,L a})\text{SnO}_3$ system, the conductivity value in the high doping regions above $n = 2 \times 10^{20} \text{ cm}^{-3}$ is $\sim 10^4 \Omega^{-1}\text{cm}^{-1}$ in the single crystal at room temperature (Fig. 4 (a)), which is close to the highest value among the transparent conductors. The best conductivity of the $\text{In}_2\text{O}_3:\text{Sn}$ is known to be $\sim 10^4 \Omega^{-1}\text{cm}^{-1}$. Thus, $(\text{Ba,L a})\text{SnO}_3$ can be also used as transparent conductors.

To understand further detailed electrical transport properties, we performed the temperature-dependent resistivity measurements as summarized in Fig. 5. First, we note that the carrier densities are almost temperature-independent in both single crystals and films (Figs. 5 (a) and (b)). In the case of the thin films, there exists a slight decrease of carrier density at low temperatures for the nominal doping $x = 0.07$. The resistivity data exhibit mostly metallic behavior, indicating that all the materials

are in a degenerately doped semiconducting regime. The resistivity values of the single crystals decrease nearly by a factor of two upon being cooled from room temperature to 2 K (Fig. 5 (e)), which then results in the increase of the corresponding mobility by the same factor (Fig. 5 (c)). The mobility increases at low temperatures seem to be a common property of both crystals and films. The factor of the resistivity decrease from room temperature to 2 K, as observed in the films with $x = 0.04$ and 0.07 , is also reflected in the increase in the corresponding mobility (Fig. 5 (d)). On the other hand, it is found that the residual resistivity values of the films are more than one order of magnitude larger than those of the crystals (Fig. 5 (f)), implying that there exist extra-scattering sources in the films such as grain boundaries and/or dislocations.

D. Optical properties

Figure 6 compares the transmission spectra for the two single crystals, undoped BaSnO₃ and (Ba, La)SnO₃ with $n = 2.39 \times 10^{20} \text{ cm}^{-3}$. Transmittance of the BaSnO₃ single crystal reaches as high as 0.71 in the visible spectral region (1.8-3.1 eV) although its thickness of 68.7 μm is rather high. The significant suppression of the transmittance near 3.1 eV reflects the development of an optical gap. According to the band calculation in Fig. 3, BaSnO₃ is an indirect gap semiconductor, in which the conduction band minimum and the valence band maximum have predominant Sn 5s and O 2p characters, respectively. The band gap of BaSnO₃ estimated from the band structure in Fig. 3 is approximately 1 eV, which is much smaller than the actual optical gap of 3.1 eV. It is rather well-known that the gap predicted by the band calculation based on the LDA approximation underestimates the actual gap in many transparent oxide materials because the LDA calculation doesn't take into account the electron correlation effect properly. Even the well-known TCO, In₂O₃:Sn exhibits a similar kind of discrepancy between the LDA calculation and the experimentally measured gap³⁷. In the case of In₂O₃:Sn, the optical gap was also clearly larger by about 0.1 eV than the gap measured by the photoemission and X-ray emission spectroscopy, which was attributed to a

combination of dipole forbidden optical transitions and conduction band occupation.⁴¹ Therefore, it will be also interesting to study in the future how the optical gap of BaSnO₃ can be also enhanced as compared to the LDA result. In other words, it will be worthwhile to check whether BaSnO₃ can also meet such a selection rule or how much electron correlation effects exist to result in the actual optical gap.

As the doping level of a single crystal increases, the transmittance is suppressed down to ~ 0.2 in the visible region as shown in Fig. 6 (a), indicating the development of the in-gap states. However, it is noted that the transmittance level in the single crystal remains finite albeit it is rather thick ($\sim 53.7 \mu\text{m}$) and has a high doping level of $n = 2.39 \times 10^{20} \text{ cm}^{-3}$. Figure 6 (b) shows the resultant α spectra of the undoped and doped single crystals as a function of photon energy. α value of the doped single crystal in the visible spectral region is still less than 300 cm^{-1} , predicting that the doped sample should have transmittance of about 0.8 in e.g., a thin film having thickness about 100 nm. This high transparency has been also observed in previous optical studies on the thin films grown on SrTiO₃ substrates²⁶. Finally, it is noted that the increase of the optical gap in the doped samples can be understood as the Burstein-Moss shift,^{42,43} which is often observed in degenerate semiconductors.

E. Debye temperatures

To extract the information on the Debye temperature, we used two methods, i.e., the thermal expansion and heat capacity measurements. Figure 7 (a) displays the evolution of temperature-dependent lattice constant of a Ba_{0.999}La_{0.001}SnO₃ polycrystalline specimen. Upon increasing the temperature, the lattice parameter increases, consistent with lattice expansion due to anharmonic thermal vibration. To model the thermal expansion data of Ba_{0.999}La_{0.001}SnO₃, we assumed that the Debye model can successfully explain the intrinsic energy of the lattice and thus its temperature-dependent expansion as well.⁴⁴ Then, the temperature dependencies of the lattice parameter (a) can be described by:⁴⁴

$$a = a_0 + bT\left(\frac{T}{\theta_D}\right)^3 \int_0^{T/\theta_D} \frac{x^3}{e^x-1} dx \quad (3)$$

, where a_0 and θ_D are the lattice constant at 0 K and Debye temperature, respectively. A solid line in Fig. 7 (a) shows the fitting result based on the above equation and the best fit was obtained when the Debye temperature is 365 K.

Figure 7 (b) shows the specific heat of a BaSnO₃ single crystal at temperatures between 2 and 330 K. For the heat capacity analysis, we adopted the two Debye phonon modes because one phonon mode alone could not fully explain the experimental data. Based on the Debye theory, the temperature dependent specific heat coming from the two phonon contributions can be described as follows:⁴⁵

$$C_v = 9qNk_B \left[x\left(\frac{T}{\theta_{\text{low}}}\right)^3 \int_0^{T/\theta_{\text{low}}} \frac{x^3}{e^x-1} dx + y\left(\frac{T}{\theta_{\text{high}}}\right)^3 \int_0^{T/\theta_{\text{high}}} \frac{x^3}{e^x-1} dx \right] \quad (4)$$

, where θ_{low} and θ_{high} are the Debye temperatures of each phonon mode, and x and y are the weights of the phonon modes. Open circles represent the temperature-dependent specific heat data of the BaSnO₃ single crystal while the lines refer to the two phonon mode contributions (dotted lines) and their sum (solid line). The model fitting can successfully explain the experimental data and the resultant two Debye temperatures θ_{low} and θ_{high} are found to be 307 K and 950 K, respectively. The resultant x/y ratio is around 1.5, implying that the heat capacity below 300 K is mainly governed by the low energy Debye phonon. When the C_p/T vs. T^2 curve is plotted at the low temperature region below 10 K, the slope yielded the Debye temperature around 280 K, confirming again that the single Debye phonon mode located around 300 K dominates the phonon population of BaSnO₃ at the low temperatures.

IV. DISCUSSION

The electrical mobility (μ) in a simple one band model is expressed by an electron effective mass (m^*) and a total electron scattering rate (τ^{-1}):

$$\mu = e\tau/m^*, \quad (1)$$

where e is an electron charge. Therefore, a high mobility can be realized with a small electron effective mass and a small total electron scattering rate. In the followings, we discuss the origins for achieving such a high mobility in (Ba,La)SnO₃ based on the peculiar characteristics reflected in the two key physical parameters, i.e., electron scattering rate and effective mass.

A. High mobility in the crystals and thin films

Controlling impurity scattering seems to be important to obtain the highest mobility of ~ 320 cm²(Vs)⁻¹ in (Ba,La)SnO₃ single crystals as observed in our previous study²⁸ and 200- 300 cm²(Vs)⁻¹ as found in this work. It was recently reported that single crystals grown by PbO + PbF₂ flux produced a mobility³⁰ close to 103 cm²(Vs)⁻¹ at a doping level $\sim 8 - 10 \times 10^{19}$ cm⁻³. As the Pb impurity can enter both Ba and Sn sites in this flux, the observation of lower mobility implies that the presence of the additional impurity other than La might lead to the increased dopant scattering. As mentioned in Sec. III A, the absence of Cu impurity in our single crystals should be then helpful in reducing the additional impurity scattering and obtaining physical properties close to the intrinsic ones.

In the thin films, it is interesting to note that a previous study found the mobility to be at best 0.69 cm²(Vs)⁻¹ although the reported films were epitaxially grown on the same type of substrate, SrTiO₃ (001)^{26,27}, as the present work. The FWHM in the rocking curve was 0.57° in the previous study while it is 0.09° in our study (Fig. 1 (d)), which represents a conspicuous improvement in the crystallinity. Therefore, the highest electrical mobility of ~ 70 cm²(Vs)⁻¹ realized in our thin films is most likely to be associated with the superior structural properties.

On the other hand, the highest mobility of ~ 70 cm²(Vs)⁻¹ in our films is still much lower than the values in the single crystals. Even though our films were epitaxially grown, we found from the transmission electron microscopy study that there exist significant grain boundaries and threading dislocations, due to the large lattice mismatch (more than 4%) between the substrate and (Ba,La)SnO₃. Those grain boundaries/dislocations are expected to act as double-Schottky barriers for the electron

transport,^{46,47} thereby giving rise to lower electrical mobility and higher residual resistivity than single crystals as demonstrated in Fig. 5. Therefore, it is expected that the mobility in thin films will be further improved when the dislocation density gets reduced by, e.g., using BaSnO₃ single crystal substrates.

Related to the presence of such grain boundaries/dislocations, the room temperature carrier densities in the films with nominal doping concentration $x = 0.01, 0.04, \text{ and } 0.07$ are $7.0 \times 10^{19} \text{ cm}^{-3}$, $4.0 \times 10^{20} \text{ cm}^{-3}$, and $6.8 \times 10^{20} \text{ cm}^{-3}$, respectively. The activation rates of dopants then become 45, 69, and 67 %, respectively. The lower activation rate for the lowest doping indicates existence of the enhanced charge trapping mechanism. Moreover, as evident in Fig. 5 (d), the mobility is reduced significantly when carrier density is decreased.²⁸ This observation implies that the higher carrier density effectively reduces the effect of dislocation/grain boundary scattering. Once the double Schottky barrier is formed in the films, the higher carrier density is likely to induce thinner barrier width and smear out the barriers, resulting in enhanced mobility up to around $n \sim 4 \times 10^{20} \text{ cm}^{-3}$. However, as the doping rate becomes higher than $4 \times 10^{20} \text{ cm}^{-3}$, the scattering by ionized dopants seems to start dominating rather than dislocations or grain boundaries, to induce a mobility decrease by the increased dopant level.

B. Effective mass

To understand the high mobility observed in the (Ba,La)SnO₃ single crystals within the band structure framework, one should expect quite a small effective mass. As mentioned in the LDA calculation results (Sec. III B), the effective masses of BaSnO₃ and (Ba,La)SnO₃ are predicted to be $\sim 0.4m_0$. It turns out that the value of $\sim 0.4m_0$ is comparable to, but not particularly smaller than the theoretically predicted effective masses of other wide-band-gap oxide semiconductors, e.g., In₂O₃ ($0.30m_0$),⁴⁸ SnO₂ ($0.38m_0$),⁴⁹ and ZnO ($0.24m_0$).⁵⁰ On the other hand, there is also a recent report based on the LDA + GGA (generalized gradient approximation) calculations that a theoretical m^* of BaSnO₃ ($0.06m_0$)⁵¹ is much smaller than that of SnO₂ ($0.38m_0$).⁴⁹ Therefore, to pin down whether the

effective mass is a dominant quantity for creating the high mobility or not, it would be necessary to determine experimentally an effective mass of (Ba,La)SnO₃.

C. Effects of various scattering in the crystal

Another key physical quantity to determine the electrical mobility is the electron scattering rate, which can be expressed by a sum of several scattering rates, according to Matthiessen's rule:

$$\tau^{-1} = \sum \tau_i^{-1} \quad (2)$$

, where τ_i^{-1} are the electron scattering rates from different scattering sources. In the single crystals of (Ba,La)SnO₃ with minimized extrinsic scattering sources, e.g., defects, the electron-phonon and ionized-dopant scatterings are likely to be main sources of the electron scattering. It is generally known that the ionized-dopant scattering in the degenerately doped regime is almost temperature independent. Then, the majority of the temperature-dependent scattering can be attributed to the electron-phonon scattering in the (Ba,La)SnO₃ system, in which the degenerately doped regime is clearly realized when the doping rate is higher than $1.0 \times 10^{19} \text{ cm}^{-3}$. For example, the temperature-dependent resistivity variation should be then determined by the electron-phonon scattering as the carrier density is mostly temperature-independent (Fig. 4 (b)).

The Debye temperature should be closely related to the electron-phonon scattering strength, as the electron-phonon scattering will increase with the number of thermally activated phonons; e.g., a smaller Debye temperature will result in a higher amount of phonon population at a given temperature. The Debye temperature of (Ba,La)SnO₃ is $\sim 365 \text{ K}$ as determined by the thermal expansion rate of lattice, and $\sim 307 \text{ K}$ as determined by the specific heat measurement. These values are indeed a bit lower than the known Debye temperatures of In₂O₃ (420 K),⁵² SnO₂ (500 K),⁵² and, ZnO (399.5 K).⁵³ Therefore, it is expected that the electron-phonon scattering in (Ba,La)SnO₃ is not particularly smaller to cause the higher mobility than those of the other transparent electronic materials.

Another important contribution to the total scattering rate is the ionized-dopant scattering. In (Ba,La)SnO₃, the La³⁺ dopants are the main ionized impurities. In a degenerately doped semiconductor, the mobility due to the ionized impurity (μ_{ii}) can be expressed as:⁵⁴

$$\mu_{ii} = \frac{3(\epsilon_r \epsilon_0)^2 h^3 n}{Z^2 m^{*2} e^3 N_i F_{ii}(\xi_d)} \quad \text{and} \quad \xi_d = (3\pi^2)^{1/3} \frac{\epsilon_r \epsilon_0 h^2 n^{1/3}}{m^* e^2} \quad (5)$$

, where the screening function $F_{ii}(\xi_d)$ is given by:

$$F_{ii}(\xi_d) = \ln(1 + \xi_d) - \frac{\xi_d}{1 + \xi_d}. \quad (6)$$

Here, h is Planck's constant, N_i is a number of ionized dopant, and ϵ_r is a dielectric constant. Equation (5) predicts that in the ionized impurity scattering regime, μ_{ii} is generally proportional to the square of the dielectric constant. We should note that the dielectric constant of BaSnO₃ (about 20)⁵⁵ is almost two times larger than the well-known transparent electronic materials; In₂O₃ (about 9), SnO₂ (9.6 - 13.5), and ZnO (8.75 - 7.8).⁵⁴ Therefore, the high mobility state in (Ba,La)SnO₃ may be due to greatly reduced ionized-dopant scattering, coming from the enhanced screening strength associated with the high dielectric constant.

Another important factor to reduce the ionized-dopant scattering should be the capability of doping the La dopant into the Ba site. It is expected that the ionized-dopant scattering should be greatly reduced if the dopant is located away from the SnO₂ layers that are the main conduction channels. This would be favorable for realizing almost defect-free SnO₂ layers. Empirical comparison of the residual resistivity supports this reasoning. The residual resistivity of the Ta doped SnO₂ was ~ 0.83 m Ω cm, at $n = \sim 1 \times 10^{20}$ cm⁻³,³⁹ which is seven times larger than that of (Ba,La)SnO₃ single crystal, ~ 0.12 m Ω cm at $n = 1.18 \times 10^{20}$ cm⁻³ (Fig. 5). Thus, it may be concluded that the location of La dopant away from the SnO₂ layers plays an important role to minimize the ionized-dopant scattering as well.

One caveat in applying equation (5) to understand the ionized-dopant scattering in our single crystals lies in the screening function $F_{ii}(\xi_d)$. Once the ionized impurity level (N_i) and actual carrier density (n) are proportional to each other, μ_{ii} is inversely proportional to $F_{ii}(\xi_d)$. In general, $F_{ii}(\xi_d)$ increases as the

carrier density increases so that one should expect a reduced μ_{fi} with increase of n in the ionized-dopant scattering regime. However, the new result in Fig. 4 (b) is not yet decisive to draw a conclusion whether the mobility indeed shows any dependence on n . The mobility values near the same carrier density level exhibit large scatter. This indicates that the single crystals are not yet perfect so that they might have additional scattering sources such as oxygen vacancies. If the oxygen vacancies are present in the middle of the conduction channel (SnO_2 layers), they can act as stronger scattering centers than the La^{3+} ions. Moreover, the actual carrier density can be also fluctuating inside a single crystal or over different pieces, possibly resulting in the scattered mobility and carrier density as seen in Fig. 4 (b). In light of the very small oxygen diffusion constant in BaSnO_3 material system, as we reported previously,²⁸ full and uniform oxygenation of mm-thick crystals may be difficult. Further studies are underway to reduce such additional scattering sources.

V. CONCLUSIONS

We found a high electrical mobility in the transparent perovskite material, $(\text{Ba},\text{La})\text{SnO}_3$. The $(\text{Ba},\text{La})\text{SnO}_3$ single crystals grown by the Cu_2O flux method showed an electrical mobility of 200-300 $\text{cm}^2(\text{Vs})^{-1}$ in a broad doping range from 1.0×10^{19} to $4.0 \times 10^{20} \text{ cm}^{-3}$, constituting the highest value among the known transparent electronic materials, such as doped In_2O_3 , SnO_2 , and ZnO . In the thin films grown epitaxially on SrTiO_3 (001), the maximum mobility reached only $\sim 70 \text{ cm}^2(\text{Vs})^{-1}$ due to the presence of dislocations/grain boundaries, which points out the possibility of enhancing the mobility in the thin film form upon having a proper substrate material. We discussed that the high mobility can arise from several unique physical conditions of $(\text{Ba},\text{La})\text{SnO}_3$: highly dispersive Sn $5s$ band coming from an ideal Sn-O-Sn bonding angle close to 180° and minimized ionized-dopant scattering from the high dielectric constant and the capability of putting La^{3+} dopant away from the main SnO_2 layer. Moreover, it is noteworthy that such a high mobility is linked to the high conductivity $\sim 10^4 \text{ } \Omega^{-1}\text{cm}^{-1}$ at room temperature at a doping level of $n = 2 \times 10^{20} \text{ cm}^{-3}$, which is

comparable to the highest value among the transparent conducting oxides. Therefore, combined with the thermal stability of the oxygen diffusion, the (Ba,La)SnO₃ system offers an unprecedented opportunity for realizing all perovskite based, transparent high-frequency, high-power functional devices.

ACKNOWLEDGEMENTS

We thank Tae Won Noh, Yun Daniel Park, and Tak Hee Lee for discussions. We acknowledge support from the NRF through Accelerated Research Program (R17-2008-33-01000-0) and through the Creative Research Initiative (2010-0018300), and by MKE through the Fundamental R&D program for Core Technology of Materials.

†Correspondence and requests for materials should be addressed to Kee Hoon Kim (khkim@phya.snu.ac.kr) and Kookrin Char (kchar@phya.snu.ac.kr).

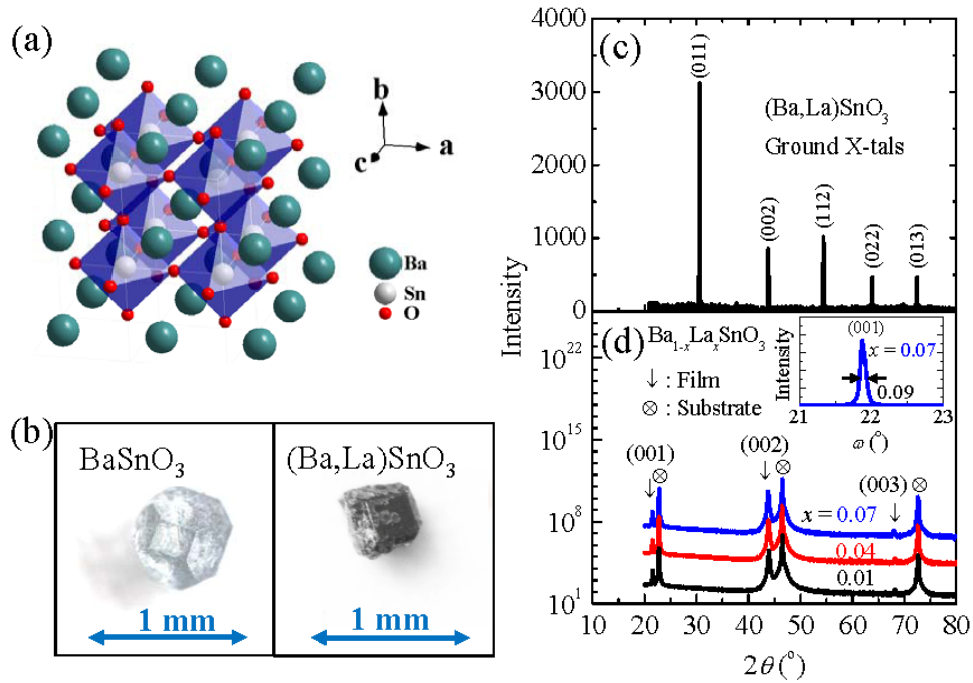


FIG. 1. (color online) (a) $2 \times 2 \times 2$ unit cells of cubic perovskite BaSnO_3 . (b) Optical microscope images of the flux grown BaSnO_3 and $(\text{Ba,La})\text{SnO}_3$. (c) X-ray θ - 2θ scan result of a $(\text{Ba,La})\text{SnO}_3$ single crystal show a single phase in the cubic perovskite structure. (d) X-ray θ - 2θ scan results show the $(00l)$ peaks in epitaxial thin films grown on SrTiO_3 (001) substrate. The inset figure shows that the full width at half maximum of the ω -scan rocking curve is only 0.09° .

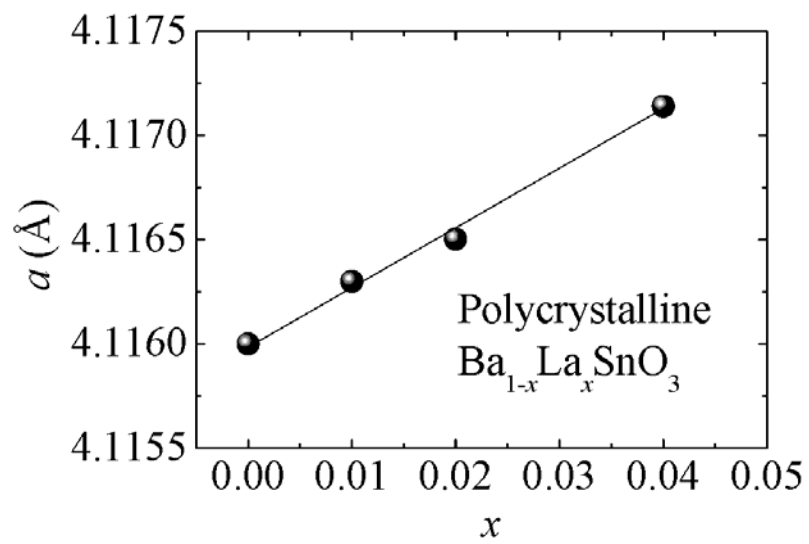


FIG. 2. (a) Cubic lattice parameter for polycrystalline $\text{Ba}_{1-x}\text{La}_x\text{SnO}_3$ ($x = 0, 0.01, 0.02, \text{ and } 0.04$) measured at RT. Line is drawn as a guide to the eye.

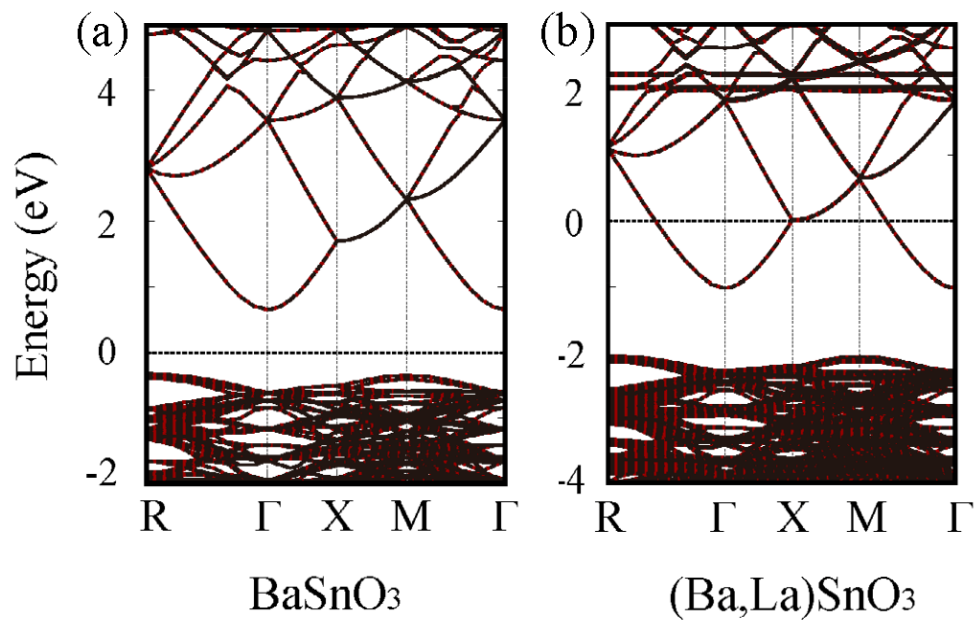


FIG 3. The band structure of (a) BaSnO₃ and (b) (Ba,La)SnO₃ obtained by first-principles calculations with 27 (3×3×3) unit cells. For (Ba,La)SnO₃, one of Ba²⁺ ions is substituted by a La³⁺ ion corresponding to the doping rate of $x=0.037$ in Ba_{1-x}La_xSnO₃.

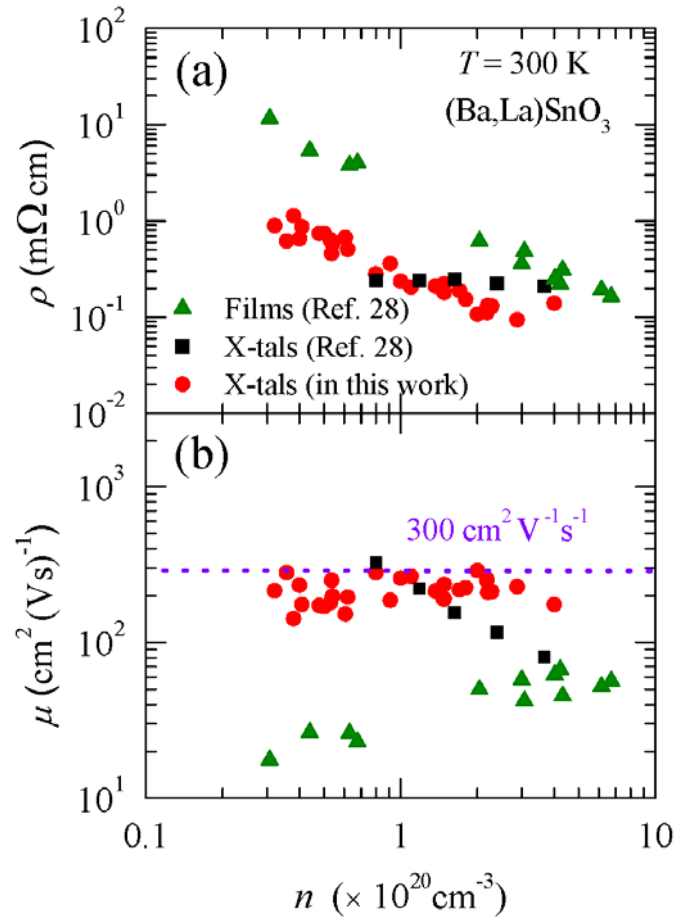


FIG. 4. (color online) (a) Resistivity (ρ) and (b) mobility (μ) vs. carrier density (n) plot. closed (black) squares and (green) triangles are for the reported single crystals and films²⁸, respectively. Closed (red) circles are for the data of single crystals in this work.

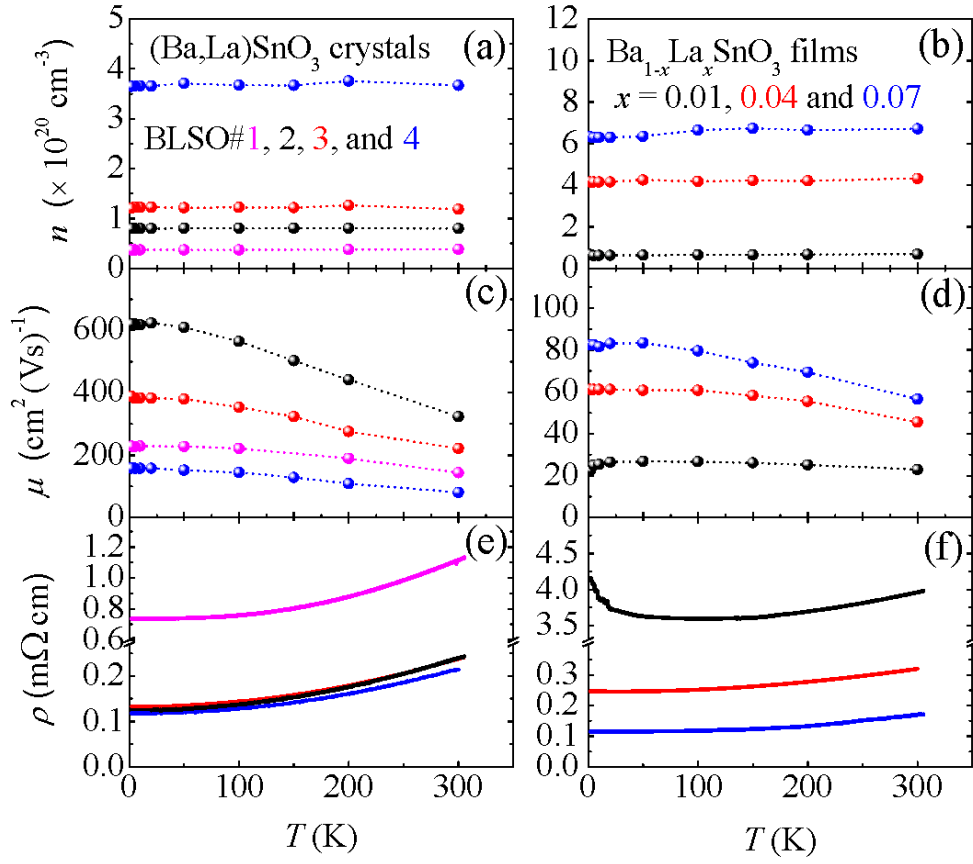


FIG. 5. (color online) Temperature-dependent carrier density n , resistivity ρ , and mobility μ are plotted for selected (Ba,Lu)SnO₃ single crystals (BLSO #1, 2, 3, and 4) (a,c,e) and thin films (b,d,f). The nominal La composition (x) is presented for the thin films.

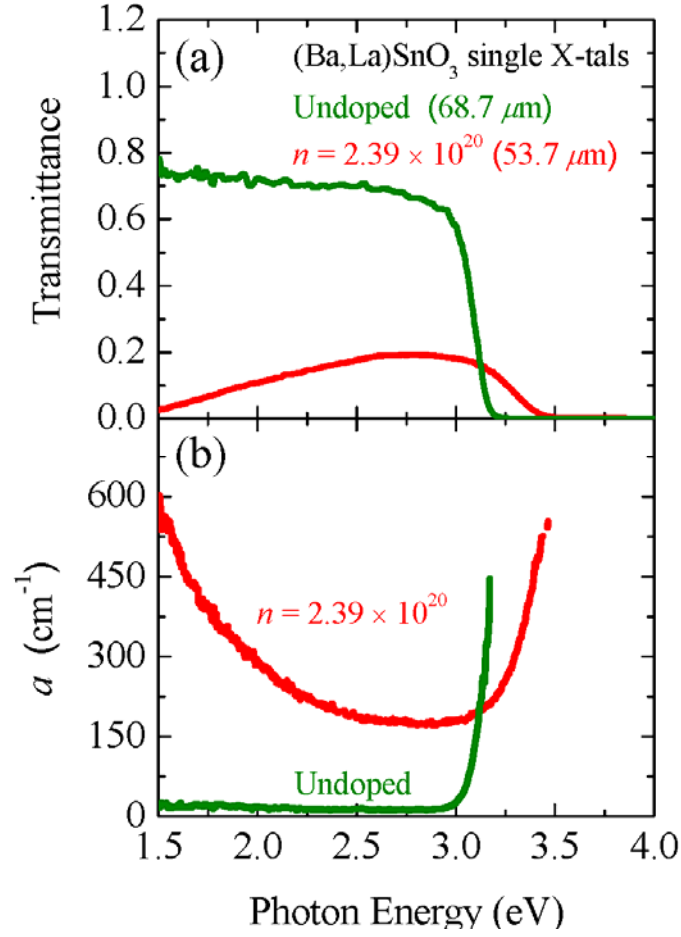


FIG. 6. (color online) (a) Transmission spectra and (b) absorption coefficient (α) of BaSnO₃ (BSO) and (Ba,L)SnO₃ single crystals are plotted as a function of photon energy. Absorption coefficient α for each undoped and doped sample ($n = 2.39 \times 10^{20} \text{ cm}^{-3}$) was extracted by measurements of transmission spectra of the same specimen in two different thicknesses.

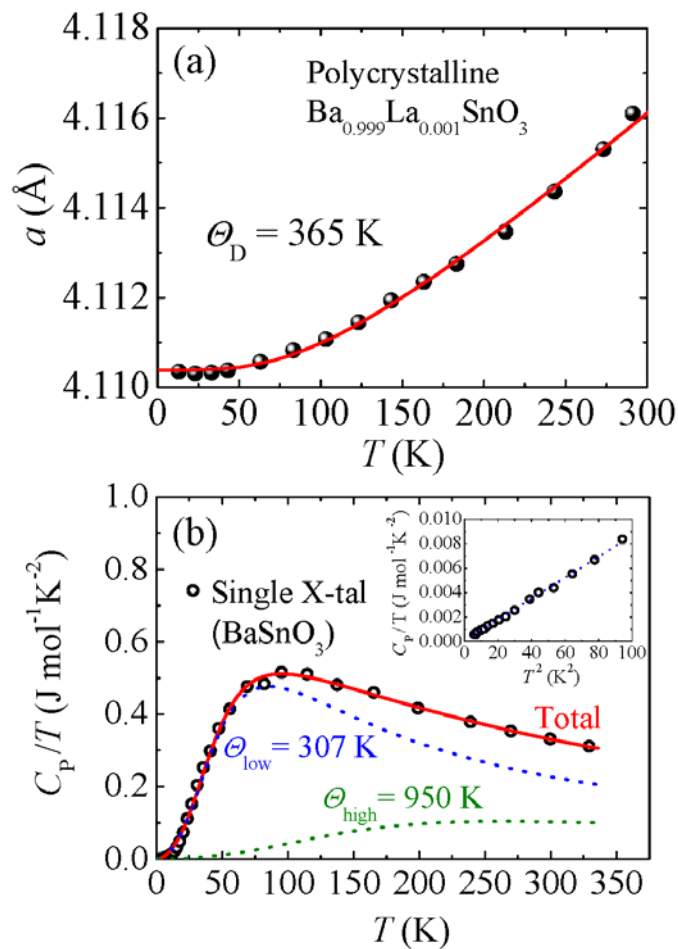


Fig. 7 (color online) (a) Thermally induced cubic lattice parameter expansion of polycrystalline $\text{Ba}_{0.999}\text{La}_{0.001}\text{SnO}_3$. The solid (red) line is the thermal expansion fitting which is based on the Debye model. (b) Open circles are the temperature dependent specific heat of BaSnO_3 single crystal. The dotted lines are two phonon mode contributions (blue and green) and the solid line refers to their sum (red). The inset figure shows the C_p/T vs. T^2 plot at low temperatures.

REFERENCES

1. D. S. Ginley and C. Bright, MRS Bull. **25**, 15 (2000).
2. A. J. Freeman, K. R. Poeppelmeier, T. O. Mason, R. P. H. Chang, and T. J. Marks, MRS Bull. **25**, 45 (2000).
3. T. Minami, MRS Bull. **25**, 38 (2000).
4. H. Hosono, Thin Solid Films **515**, 6000 (2007).
5. Z. K. Tang, G. K. L. Wong, P. Yu, M. Kawasaki, A. Ohtomo, H. Koinuma, and Y. Segawa, Appl. Phys. Lett. **72**, 3270 (1998).
6. H. Ohta, M. Orita, M. Hirano, H. Tanji, H. Kawazoe, and H. Hosono, Appl. Phys. Lett. **76**, 2740 (2000).
7. T. Makino, Y. Segawa, A. Tsukazaki, A. Ohtomo, and M. Kawasaki, Appl. Phys. Lett. **87**, 022101 (2005).
8. K. Nomura, H. Ohta, K. Ueda, T. Kamiya, M. Hirano, and H. Hosono, Science **300**, 1269 (2003)
9. R. J. Cava, B. Batlogg, J. J. Krajewski, R. Farrow, L. W. Rupp Jr, A. E. White, K. Short, W. F. Peck, and T. Kometani , Nature **332**, 814 (1988).
10. Y. Tokura and Y. Tomioka, J. Magn. Magn. Mater. **200**, 1 (1999).
11. G. H. Haertling, J. Am. Ceram. Soc. **82**, 797 (1999).
12. T. Kimura, T. Goto, H. Shintani, K. Ishizaka, T. Arima, and Y. Tokura, Nature **426**, 55 (2003).
13. C. H. Ahn, J.-M. Triscone, and J. Mannhart, Nature **424**, 1015 (2003).
14. H.-H. Wang, D.-F. Cui, S.-Y Dai, H.-B. Lu, Y.-L. Zhou, Z.-H. Chen, and G.-Z. Yang, J. Appl. Phys. **90**, 4664 (2001).
15. H. Guo, L. Liu, Y. Fei, W. Xiang, H. Lü, S. Dai, Y. Zhou, and Z. Chen, J. Appl. Phys. **94**, 4558 (2003).
16. J. H. Cho and H. J. Cho, Appl. Phys. Lett. **79**, 1426 (2001).
17. R. P. Wang and C. J. Tao, J. Crys. Growth **245**, 63 (2002).

18. H. Tetsuka, Y. J. Shan, K. Tezuka, H. Imoto and K. Wasa, *J. Vac. Sci. Technol. A* **24**, L4 (2006).
19. B. Hadjarab, A. Bouguelia, and M. Trari, *J. Phys. Chem. Solids* **68**, 1491 (2007).
20. P. Singh, D. Kumar, and O. Parkash, *J. Appl. Phys.* **97**, 074103 (2005).
21. U. Lampe, J. Gerblinger, and H. Meixner, *Sens. Actuators, B*, **24-25**, 657 (1995).
22. H. Mizoguchi, H. W. Eng, and P. M. Woodward, *Inorg. Chem.* **43**, 1667 (2004).
23. T. Huang, T. Nakamura, M. Itoh, Y. Inaguma, and O. Ishiyama, *J. Mater. Sci.* **30**, 1556 (1995).
24. R. J. Cava, P. Gammel, B. Batlogg, J. J. Krajewski, W. F. Peck, Jr., L. W. Rupp, Jr., R. Felder, and R. B. van Dover, *Phys. Rev. B* **42**, 4815 (1990).
25. M. Yasukawa, T. Kono, K. Ueda, H. Yanagi, H. Hosono, *Mater. Sci. Eng. B.* **173**, 29 (2010).
26. H. F. Wang, Q. Z. Liu, F. Chen, G. Y. Gao, W. Wu, and X. H. Chen, *J. Appl. Phys.* **101**, 106105 (2007).
27. Q. Liu, J. Dai, Z. Liu, X. Zhang, G. Zhu, and G. Ding, *J. Phys. D: Appl. Phys.* **43**, 455401 (2010).
28. H. J. Kim, U. Kim, H. M. Kim, T. H. Kim, H. S. Mun, B.-G. Jeon, K. T. Hong, W.-J. Lee, C. Ju, K. H. Kim, and K. Char, *Appl. Phys. Express* **5**, 061102 (2012).
29. H. J. Kim, J. Kim, W. S. Choi, D. W. Jeong, J. Yu, T. W. Noh, and K. H. Kim, 2012 MRS Spring Meeting & Exhibit G9.12/S8.12
30. X. Luo, Y. S. Oh, A. Sirenko, P. Gao, T. A. Tyson, K. Char, and S.-W. Cheong, *Appl. Phys. Lett.* **100**, 172112 (2012).
31. G. Kresse and J. Furthmüller, *Phys. Rev. B* **54**, 11169 (1996).
32. P. E. Blöchl, *Phys. Rev. B* **50**, 17953 (1994).
33. D. M. Ceperley and B. J. Alder, *Phys. Rev. Lett.* **45**, 566 (1980).
34. R. Bachmann, F. J. DiSalvo, Jr., T. H. Geballe, R. L. Greene, R. E. Howard, C. N. King, H. C. Kirsch, K. N. Lee, R. E. Schwall, H.-U. Thomas, and R. B. Zubeck, *Rev. Sci. Instrum.* **43**, 205 (1972).
35. J. S. Hwang, K. J. Lin, and C. Tien, *Rev. Sci. Instrum.* **68**, 94 (1997).

36. R. D. Shannon, *Acta Cryst. A* **32**, 751 (1976).
37. O. N. Mryasov and A. J. Freeman, *Phys. Rev. B* **64**, 233111 (2001).
38. R. L. Weiher, *J. Appl. Phys.* **33**, 2834 (1962).
39. H. Toyosaki, M. Kawasaki, and Y. Tokura, *Appl. Phys. Lett.* **93**, 132109 (2008).
40. A. Ohtomo, K. Tamura, K. Saikusa, K. Takahashi, T. Makino, Y. Segawa, H. Koinuma, and M. Kawasaki, *Appl. Phys. Lett.* **75**, 2635 (1999).
41. A. Walsh, J. L. F. Da Silva, S.-H. Wei, C. Körber, A. Klein, L. F. J. Piper, A. DeMasi, K. E. Smith, G. Panaccione, P. Torelli, D. J. Payne, A. Bourlange, and R. G. Egdell, *Phys. Rev. Lett.* **100**, 167402 (2008).
42. E. Burstein, *Phys. Rev.* **93**, 632 (1954).
43. T. S. Moss, *Proc. Phys. Soc. (London)* **B67**, 775 (1954).
44. C. Roder, S. Einfeldt, S. Figge, and D. Hommel. *Phys. Rev. B* **72**, 085218 (2005).
45. A. D. Fortes, I. G. Wood, J. P. Brodholt, M. Alfredsson, L. Vočadlo, G. S. McGrady, and K. S. Knight, *J. Chem. Phys.* **119**, 10806 (2003).
46. M. Vollman and R. Waser, *J. Am. Ceram. Soc.* **77**, 235 (1994).
47. K. Ellmer and R. Mientus, *Thin Solid Films* **516**, 4620 (2008).
48. H. Odaka, S. Iwata, N. Taga, S. Ohnishi, Y. Kaneta, and Y. Shigesato, *Jpn. J. Appl. Phys.* **36**, 5551 (1997).
49. P. D. Borges, L. M. R. Scolfaro, H. W. L. Alves and E. F. da Silva, Jr., *Theor. Chem. Acc.* **126**, 39 (2010).
50. M. Oshikiri, Y. Imanaka, F. Aryasetiawan, and G. Kido, *Physica B* **298**, 472 (2001).
51. E. Moreira, J. M. Henriques, D. L. Azevedo, E. W. S. Caetano, V. N. Freire, and E. L. Albuquerque, *J. Solid State Chem.* **187**, 186 (2012).
52. K. J. Bachmann, F.S.L. Hsu, and J. P. Remeika, *Phys. Stat. Sol. (a)* **67**, K39 (1981).
53. W. N. Lawless and T. K. Gupta, *J. Appl. Phys.* **60**, 607 (1986).
54. K. Ellmer, *J. Phys. D: Appl. Phys.* **34** 3097 (2001).

55. P. Singh, B. J. Brandenburg, C. P. Sebastian, P. Singh, S. Singh, D. Kumar, and O. Parkash, *Jpn. J. Appl. Phys.* **47**, 3540 (2008).